Journals of the Japan Society of Mechanical Engineers

Lattice Boltzmann simulation of motion of red blood cell in constricted circular pipe flow

--Manuscript Draft--

Manuscript Number:	JOURNAL-JSME-D-14-00133R2
Full Title:	Lattice Boltzmann simulation of motion of red blood cell in constricted circular pipe flow
Article Type:	Original Paper (JSME Journals)
Manuscript Classifications:	Liquid-Solid Two-Phase Flow (固液二相流); Microfluidics (マイクロフルイディックス); Multi-phase Flow (混相流); Numerical Simulation (数値シミュレーション); Lattice-Bolt z man method (格子ボルツマン法)
Corresponding Author:	Masato Yoshino, Ph.D. Engineering Nagano, JAPAN
Corresponding Author Secondary Information:	正人 吉野
Corresponding Author's Institution:	Engineering
Corresponding Author's Secondary Institution:	信州大学
First Author:	Masato Yoshino, Ph.D.
First Author Secondary Information:	正人 吉野
Order of Authors:	Masato Yoshino, Ph.D.
	Shingo Katsumi
Order of Authors Secondary Information:	正人 吉野
Abstract:	The lattice Boltzmann method for two-phase flows containing a deformable body with a viscoelastic membrane is improved to simulate circular pipe flows by incorporation of the immersed boundary method. In order to examine the validity of the red blood cell (RBC) model, the method is applied to the motion of a biconcave disk-shaped body in a pressure-driven circular pipe flow. The validation is demonstrated by investigating the relation between the deformation index and terminal axial velocity of the RBC in the pipe flow. In this study, the behavior of a biconcave disk-shaped body in constricted pipe flows is simulated under various geometrical conditions. The square and circular pipes with various lengths and sizes of the constriction are considered, and the flow is induced by the pressure difference between the inlet and outlet. From the results, it is found that as the length of the constriction becomes smaller, the body is deformed larger and accelerated at the entrance and exit in the constriction, although the speed of the body is reduced while passing through the constriction. Also, it is found that as the size of the constriction becomes larger, the deformation index linearly decreases and the axial velocity exponentially increases. These results indicate that the present method has applicability to simulation of the motion of RBCs in microscale capillary blood vessels.
Additional Information:	
Question	**Response**
1.Are you a member of the JSME ?	Yes
Please enter your number. as follow-up to "1.Are you a member of the JSME ?"	0012082
2.Which category do you choose?	Fluids Engineering
3.Do you submit a special issue ?	Yes
Please enter a special issue name. as follow-up to "3.Do you submit a	Special Issue of the Fourth International Conference on Jets, Wakes and Separated Flows (ICJWSF2013)

special issue ?"	

Bulletin of the JSME
Vol.X, No.X, XXXX

Lattice Boltzmann simulation of motion of red blood cell in constricted circular pipe flow

Masato YOSHINO*,** and Shingo KATSUMI***
* Institute of Engineering, Academic Assembly, Shinshu University
** Institute of Carbon Science and Technology, Interdisciplinary Cluster for Cutting Edge Research, Shinshu University
*** Department of Mechanical Systems Engineering, Graduate School of Science and Technology, Shinshu University
4-17-1 Wakasato, Nagano-shi, Nagano 380-8553, Japan
E-mail: masato@shinshu-u.ac.jp

Abstract
The lattice Boltzmann method for two-phase flows containing a deformable body with a viscoelastic membrane is improved to simulate circular pipe flows by incorporation of the immersed boundary method. In order to examine the validity of the red blood cell (RBC) model, the method is applied to the motion of a biconcave disk-shaped body in a pressure-driven circular pipe flow. The validation is demonstrated by investigating the relation between the deformation index and terminal axial velocity of the RBC in the pipe flow. In this study, the behavior of a biconcave disk-shaped body in constricted pipe flows is simulated under various geometrical conditions. The square and circular pipes with various lengths and sizes of the constriction are considered, and the flow is induced by the pressure difference between the inlet and outlet. From the results, it is found that as the length of the constriction becomes smaller, the body is deformed larger and accelerated at the entrance and exit in the constriction, although the speed of the body is reduced while passing through the constriction. Also, it is found that as the size of the constriction becomes larger, the deformation index linearly decreases and the axial velocity exponentially increases. These results indicate that the present method has applicability to simulation of the motion of RBCs in microscale capillary blood vessels.

Key words : Lattice Boltzmann Method, Immersed Boundary Method, Two-Phase Flow, Red Blood Cell, Viscoelastic Membrane, Circular Pipe, Constriction

1. Introduction

Problems of the motion of viscoelastic bodies in fluid flows can be found in not only many engineering applications but also biomedical fields such as red blood cells (RBCs) in blood plasma. Normal RBCs have viscoelastic membrane and are easily deformed in small blood vessels where the cellular size is comparable to the vessel diameter. In the past, it was difficult to examine the phenomena that were involved, particularly in microscale vessels, by experimental and numerical approaches. Nevertheless, owing to the advances in measurement devices and numerical methods, many researches of the behavior of RBCs in fluid flows have been hitherto reported.

With regard to experimental studies on the behavior of RBCs in fluid flows, Hochmuth et al. (1970) investigated the motion of RBCs passing through glass capillaries of 4-10 μm diameter, and found that the longitudinal length of RBC becomes larger as the RBC velocity increases. Fischer et al. (1978) reported tank-tread like motion of human erythrocyte membrane in shear flow. Then, Tsukada et al. (2001) measured the erythrocyte deformability in vitro by making a crystal microchannel system with a high-speed video camera. In their experiments, the deformability of hardened erythrocytes (e.g., diabetic erythrocytes) is indeed measurably lower than that of usual erythrocytes in healthy controls. As for numerical simulations, Ramanujan and Pozrikidis (1998) studied the deformation of a liquid capsule enclosed by an elastic membrane in shear flows with the boundary element method. Dzwinel et al. (2003) proposed discrete particle models for simulation of RBCs in capillary vessels by the Lagrangian coordinates technique. Imai et al. (2010) have recently used the moving particle semi-implicit (MPS) method (Koshizuka and Oka, 1996), which is one of the particle methods, to

*Received DD MM, YYYY (No. XX-XXXX)
[DOI: 10.1299/XXX.X.1]

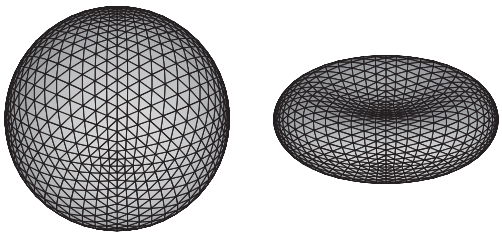

Fig. 1 Discretization of bodies: a sphere (left); a biconcave disk (right).

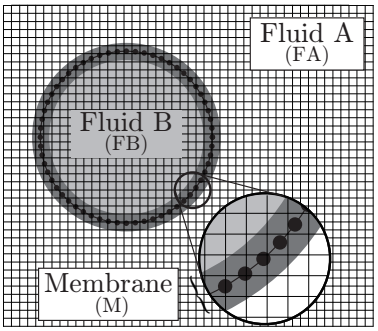

Fig. 2 Model of a body with viscoelastic membrane.

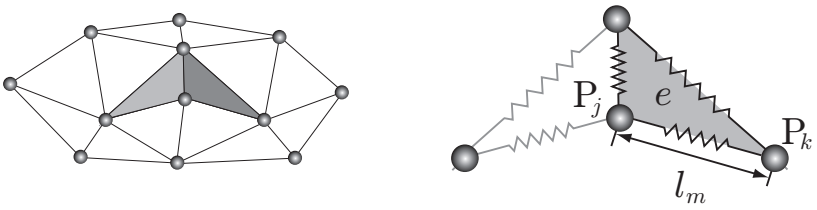

Fig. 3 Diagram of triangular mesh (left) and spring model (right).

investigate the motion of the RBC flowing into a constricted square pipe.

Over the last two decades, the lattice Boltzmann method (LBM) (Rothman and Zaleski, 1997; Chen and Doolen, 1998; Wolf-Gladrow, 2000; Succi, 2001) has been developed into an alternative and promising numerical scheme for simulating viscous fluid flows and for multicomponent and multiphase fluid flows. Sui et al. (2008) simulated the motion of a body with elastic membrane in shear flows by the LBM with the immersed boundary method (IBM) (Peskin, 1977). Dupin et al. (2008) also simulated the motion of red blood cells in fluid flows. They discretized the three-dimensional capsule membrane into flat triangular elements, and the elastic forces acting at the triangle vertices are inserted into grid points in the LBM. The authors' group (Yoshino and Murayama, 2009; Murayama et al., 2011a; Murayama et al., 2011b) has also proposed a numerical method based on the LBM to simulate behavior of a deformable body with a viscoelastic membrane in fluid flows. They confirmed the validity of the method in fundamental flow problems, and demonstrated the potential for microscale two-phase flows. However, because the method is basically formulated in Cartesian coordinates, it needs to be extended to deal with rounded boundaries such as circular pipes in order to simulate the motion of real RBCs in capillary blood vessels.

In the present paper, the above-mentioned method with the IBM at rounded boundaries is applied to the motion of a biconcave disk-shaped body in circular pipe flows. In particular, the characteristics of the body passing through a constriction are investigated under various geometrical conditions.

2. Modeling of body with viscoelastic membrane

2.1. Membrane discretization

Three-dimensional structural membrane models are discretized into flat triangular elements. The triangulation procedure is similar to those of Ramanujan and Pozrikidis (1998). To discretize the unstressed interface, each triangular face of a regular octahedron is subdivided into 4^n triangular elements, where n is a positive integer. These elements are then projected radially onto a sphere. The geometry of each element is described by its three vertices. The discretization of a spherical surface is shown in Fig. 1 (left). The biconcave disk-shaped model in Fig. 1 (right) is constructed by means of the mapping system. The mapping function and parameters are the same as those used in Sui et al. (2008).

2.2. Elastic force

Because the viscous effect of the body is inherent in the original LBM for two-phase flows, only an elastic force based on the Kelvin–Voigt model is introduced into the LBM. As shown in Fig. 2, a body with a viscoelastic membrane of a finite but relatively thin thickness is considered, where the membrane is composed of particles that are connected with their neighboring particles by springs. The body has an internal viscous fluid covered by the viscoelastic membrane. The

internal fluid is referred to as Fluid B, which is distinguished from the surrounding viscous fluid called Fluid A. Since these fluids have their own character, it is required to distinguish them in some way to give different values of physical properties. In the present model, as in Murayama et al. (2011b), these fluids are distinguished by an order parameter in the LBM for two-phase flows described later. However, the membrane is not autonomously determined but the region of the cubic lattices containing particles is assumed to be a membrane, so that the elastic force is applied to all vertices of the cubic lattices.

As shown in Fig. 3, the elastic membrane models are composed of small triangular elements connected by springs where Lagrangian particles are positioned at the vertices. A body with a viscoelastic membrane which encloses a viscous fluid has mechanical property of elastic resistances to the stretching, dilation and bending. For example, a normal RBC has strong resistance to the dilation of the body as well as to the stretching of the membrane. This is attributed to the fact that such bodies have an inherent characteristics of conserving surface area of the membrane and total volume of the body. Moreover, as reported in Evans (1980), the effect of the elastic resistance to the bending is negligibly smaller than that of the others for a thin viscoelastic membrane. Therefore, only the resistances to the stretching and dilation are introduced in the present model.

The elastic force acting on the particles is determined according to the principle of virtual work, which means that the behavior of the body is determined by moving the particles so that the total elastic energy E can lead to a minimum value. By reference to the idea of spring model by Wada and Kobayashi (2003) and Tsubota et al. (2006), the total energy E is the sum of the following quantities: the energy for the elastic resistance to the stretching of the membrane, E^{l}, the energy for the elastic resistance to the dilation of the body, $E^{\mathrm{A}} + E^{\mathrm{V}}$, where E^{A} is concerned with the surface area and E^{V} with the total volume of the body. These energies are expressed by

$$E = E^{\mathrm{l}} + E^{\mathrm{A}} + E^{\mathrm{V}}, \tag{1}$$

where

$$\left.\begin{aligned} E^{\mathrm{l}} &= \sum_{m=1}^{N_{\mathrm{s}}} \frac{1}{2} K_m^{\mathrm{l}} \left(\frac{l_m - l_{m0}}{l_{m0}} \right)^2, \\ E^{\mathrm{A}} &= \frac{1}{2} K^{\mathrm{a}} \sum_{e=1}^{N_{\mathrm{e}}} \left(\frac{A_e - A_{e0}}{A_{e0}} \right)^2 + \frac{1}{2} K^{\mathrm{A}} \left(\frac{A - A_0}{A_0} \right)^2, \\ E^{\mathrm{V}} &= \frac{1}{2} K^{\mathrm{V}} \left(\frac{V - V_0}{V_0} \right)^2. \end{aligned}\right\} \tag{2}$$

In the above equations, $l_m = \left| \boldsymbol{X}_j - \boldsymbol{X}_k \right|$ is the stretch (or compression) displacement between the neighboring two particles P_j and P_k at Lagrangian points $\boldsymbol{X}_j$ and $\boldsymbol{X}_k$ ($j, k = 1, 2, \ldots, N_{\mathrm{p}}$), A_e is the area of the element e, A is the total surface area of the membrane, V is the total volume of the body, N_{p}, N_{s} and N_{e} are the numbers of particles, springs and elements, respectively, and K_m^{l}, K^{a}, K^{A} and K^{V} are the elastic moduli for stretching of the membrane, dilation of the local surface area, dilation of the total surface area and the dilation of the total volume, respectively. Note that the subscript 0 indicates the initial value of each property.

Consequently, the elastic force $\boldsymbol{F}_j$ acting on the particle P_j at the Lagrangian point $\boldsymbol{X}_j$ is given by

$$\boldsymbol{F}_j = -\frac{\partial E}{\partial \boldsymbol{X}_j}. \tag{3}$$

3. Numerical method

As described in Inamuro (2006) and Suzuki and Inamuro (2011), we use non-dimensional variables defined by a characteristic length $\tilde{L}$, a character particle speed $\tilde{c}$, a characteristic time scale $\tilde{t}_0 = \tilde{L}/\tilde{U}$, where $\tilde{U}$ is a characteristic flow speed, a reference order parameter $\tilde{\phi}_0$ and a reference density $\tilde{\rho}_0$.

3.1. Two-phase lattice Boltzmann method

In the LBM, a modeled fluid, which is composed of identical particles whose velocities are restricted to a finite set of vectors, is considered. The three-dimensional 15-velocity model, as shown in Fig. 4, is used in the present study. This

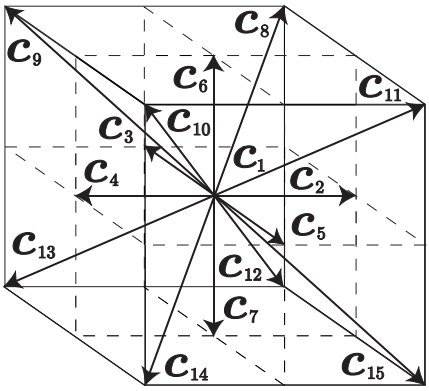

Fig. 4 Three-dimensional 15-velocity (3D15V) model.

model has the velocity vectors:

$$[\boldsymbol{c}_1, \boldsymbol{c}_2, \boldsymbol{c}_3, \boldsymbol{c}_4, \boldsymbol{c}_5, \boldsymbol{c}_6, \boldsymbol{c}_7, \boldsymbol{c}_8, \boldsymbol{c}_9, \boldsymbol{c}_{10}, \boldsymbol{c}_{11}, \boldsymbol{c}_{12}, \boldsymbol{c}_{13}, \boldsymbol{c}_{14}, \boldsymbol{c}_{15}]$$

$$= \begin{bmatrix} 0 & 1 & 0 & -1 & 0 & 0 & 0 & 1 & -1 & -1 & 1 & 1 & -1 & -1 & 1 \\ 0 & 0 & 1 & 0 & -1 & 0 & 0 & 1 & 1 & -1 & -1 & 1 & 1 & -1 & -1 \\ 0 & 0 & 0 & 0 & 0 & 1 & -1 & 1 & 1 & 1 & 1 & -1 & -1 & -1 & -1 \end{bmatrix}. \tag{4}$$

We assume two-phase fluid flows with negligibly small density difference by considering the case of human RBCs in plasma. Hence, the numerical algorithm is based on the LBM for incompressible two-phase fluids with the same density (Inamuro et al., 2003).

In the calculations, the physical domain is divided into a cubic lattice, and the evolution of particle population at each lattice point is computed. The evolution of the particle distribution functions $f_i(\boldsymbol{x}, t)$ and $g_i(\boldsymbol{x}, t)$ with velocity $\boldsymbol{c}_i$ at point $\boldsymbol{x}$ and at time t is computed by

$$f_i(\boldsymbol{x} + \boldsymbol{c}_i \Delta x, t + \Delta t) = f_i^{\mathrm{c}}(\boldsymbol{x}, t), \tag{5}$$

$$g_i(\boldsymbol{x} + \boldsymbol{c}_i \Delta x, t + \Delta t) = g_i^{\mathrm{c}}(\boldsymbol{x}, t), \tag{6}$$

where f_i^{c} and g_i^{c} are functions of macroscopic variables and their derivatives given below, and Δt is a time-step during which the particles travel the lattice spacing Δx. Note that $\Delta t = St \Delta x$, where $St = \tilde{L}/(\tilde{t}_0 \tilde{c}) = \tilde{U}/\tilde{c} = O(\Delta x)$ is the Strouhal number.

The order parameter ϕ distinguishing the two phases, the pressure p and the velocity $\boldsymbol{u}$ of the two-phase fluids are defined as follows:

$$\phi = \sum_{i=1}^{15} f_i, \tag{7}$$

$$p = \frac{1}{3} \sum_{i=1}^{15} g_i, \tag{8}$$

$$\boldsymbol{u} = \sum_{i=1}^{15} g_i \boldsymbol{c}_i. \tag{9}$$

The functions f_i^{c} and g_i^{c} in Eqs. (5) and (6) are given by

$$f_i^{\mathrm{c}} = H_i \phi + F_i \left(p_0(\phi) - \kappa_f \phi \nabla^2 \phi - \frac{\kappa_f}{6} |\nabla \phi|^2 \right) + 3 E_i \phi c_{i\alpha} u_\alpha + E_i \kappa_f G_{\alpha\beta}(\phi) c_{i\alpha} c_{i\beta}, \tag{10}$$

$$g_i^{\mathrm{c}} = E_i \left[3p + 3 c_{i\alpha} u_\alpha - \frac{3}{2} u_\alpha u_\alpha + \frac{9}{2} c_{i\alpha} c_{i\beta} u_\alpha u_\beta + \frac{3}{4} \Delta x \left(\frac{\partial u_\beta}{\partial x_\alpha} + \frac{\partial u_\alpha}{\partial x_\beta} \right) c_{i\alpha} c_{i\beta} \right]$$
$$+ 3 E_i c_{i\alpha} \frac{\partial}{\partial x_\beta} \left[\mu \left(\frac{\partial u_\beta}{\partial x_\alpha} + \frac{\partial u_\alpha}{\partial x_\beta} \right) \right] \Delta x + 3 \Delta x E_i c_{i\alpha} \delta_{\Pi \mathrm{M}} F_\alpha, \tag{11}$$

with

$$\left. \begin{aligned} &E_1 = \frac{2}{9}, \quad E_2 = E_3 = \cdots = E_7 = \frac{1}{9}, \quad E_8 = E_9 = \cdots = E_{15} = \frac{1}{72} \\ &H_1 = 1, \quad H_2 = H_3 = \cdots = H_{15} = 0, \quad F_1 = -\frac{7}{3}, \ F_i = 3E_i \ (i = 2, 3, \ldots, 15) \end{aligned} \right\} \tag{12}$$

and

$$p_0(\phi) = \phi T_\phi \frac{1}{1-b\phi} - a\phi^2, \tag{13}$$

$$G_{\alpha\beta}(\phi) = \frac{9}{2}\frac{\partial\phi}{\partial x_\alpha}\frac{\partial\phi}{\partial x_\beta} - \frac{3}{2}\frac{\partial\phi}{\partial x_\gamma}\frac{\partial\phi}{\partial x_\gamma}\delta_{\alpha\beta}, \tag{14}$$

where $\alpha, \beta, \gamma = x, y, z$ (subscripts α, β and γ indicate Cartesian coordinates and the summation convention is used), and $\Pi = \mathrm{FA}, \mathrm{FB}, \mathrm{M}$ (subscripts FA, FB and M represent fluid phase A, fluid phase B and membrane, respectively). In the above equations, $\delta_{\alpha\beta}$ is the Kronecker delta, κ_f is a constant parameter determining the width of the interface, μ is the viscosity, a, b and T_ϕ are free parameters determining the maximum and minimum values of ϕ, and F_α is the elastic force at the grid point described below. Note that the interfacial tension is assumed to be free in the present study; the constant parameter κ_g determining the strength of the interfacial tension, which appears in Inamuro et al. (2003), is set to zero in the present calculations.

For the calculation of the gradient and the Laplacian of a variable ψ in Eqs. (10), (11) and (14), the following second-order finite-difference approximations given by the Taylor series expansion are used:

$$\frac{\partial\psi}{\partial x_\alpha} \approx \frac{1}{10\Delta x}\sum_{i=2}^{15} c_{i\alpha}\psi(\boldsymbol{x} + \boldsymbol{c}_i\Delta x), \tag{15}$$

$$\nabla^2\psi \approx \frac{1}{5(\Delta x)^2}\left[\sum_{i=2}^{15}\psi(\boldsymbol{x} + \boldsymbol{c}_i\Delta x) - 14\psi(\boldsymbol{x})\right]. \tag{16}$$

As mentioned in Inamuro (2006), applying the asymptotic theory (Sone, 1971) to Eqs. (5) and (6) with appropriate initial and boundary conditions, we can obtain the phase-field advection–diffusion equation (the Cahn–Hilliard equation plus advection) for ϕ, the continuity equation and the Navier–Stokes equations for incompressible two-phase fluids.

3.2. Immersed boundary method

As described in Suzuki and Inamuro (2011), in the IBM, it is assumed that an incompressible viscous fluid is filled in both inside and outside of the boundary. Then, the body forces are applied on lattice points near the boundary in order to enforce the no-slip condition on the boundary. In the present computations, the IBM with the multi-direct forcing method (MDFM) proposed by Wang et al. (2008) is applied to the stationary curved boundary of circular pipes.

Let $\boldsymbol{X}_k(t + \Delta t)$ $(k = 1, 2, \ldots, N)$ be the Lagrangian points of the boundary. Note that the boundary velocities at the points are set to $\boldsymbol{U}_k(t + \Delta t) = \boldsymbol{0}$ for the stationary boundary. Also, note that the boundary is represented by N points, and the boundary Lagrangian points $\boldsymbol{X}_k$ generally differ from the Eulerian grid points $\boldsymbol{x}$. Then, the temporal velocities $\boldsymbol{u}^*(\boldsymbol{X}_k, t + \Delta t)$, which are calculated by using the distribution functions evolved without a body force, are interpolated by

$$\boldsymbol{u}^*(\boldsymbol{X}_k, t + \Delta t) = \sum_{\boldsymbol{x}} \boldsymbol{u}^*(\boldsymbol{x}, t + \Delta t)W(\boldsymbol{x} - \boldsymbol{X}_k)(\Delta x)^3, \tag{17}$$

where the summation symbol represents the sum over all Eulerian grid points $\boldsymbol{x}$, and W is the weighting function proposed by Peskin (2002), which is given by

$$W(x, y, z) = \frac{1}{\Delta x}w\left(\frac{x}{\Delta x}\right)\cdot\frac{1}{\Delta x}w\left(\frac{y}{\Delta x}\right)\cdot\frac{1}{\Delta x}w\left(\frac{z}{\Delta x}\right), \tag{18}$$

where

$$w(r) = \begin{cases} \dfrac{1}{8}\left(3 - 2|r| + \sqrt{1 + 4|r| - 4r^2}\right), & |r| \le 1 \\ \dfrac{1}{8}\left(5 - 2|r| - \sqrt{-7 + 12|r| - 4r^2}\right), & 1 \le |r| \le 2 \\ 0, & \text{otherwise.} \end{cases} \tag{19}$$

The body force $\boldsymbol{G}(\boldsymbol{x}, t + \Delta t)$ is determined by the following iterative procedure (Suzuki and Inamuro, 2011).

Firstly, before iteration, we compute the initial value of the body force at the boundary Lagrangian points by

$$\boldsymbol{G}_0(\boldsymbol{X}_k, t + \Delta t) = -\frac{St}{\Delta t}\boldsymbol{u}^*(\boldsymbol{X}_k, t + \Delta t), \tag{20}$$

where $St/\Delta t = 1/\Delta x$. Secondly, we compute the body force at the Eulerian grid points of ℓth iteration by

$$\boldsymbol{G}_\ell(\boldsymbol{x}, t + \Delta t) = \sum_{k=1}^{N} \boldsymbol{G}_\ell(\boldsymbol{X}_k, t + \Delta t)W(\boldsymbol{x} - \boldsymbol{X}_k)(\Delta x)^3. \tag{21}$$

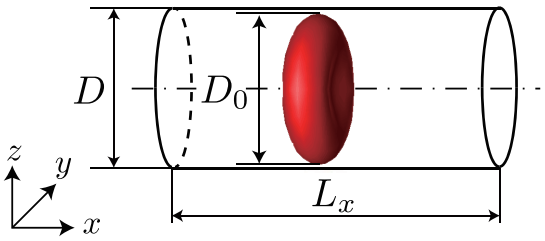

Fig. 5 Computational domain of pipe flow problem.

Thirdly, we correct the velocity at the Eulerian grid point by

$$\boldsymbol{u}_\ell(\boldsymbol{x}, t+\Delta t) = \boldsymbol{u}^*(\boldsymbol{x}, t+\Delta t) + \frac{\Delta t}{St}\boldsymbol{G}_\ell(\boldsymbol{x}, t+\Delta t). \tag{22}$$

Fourthly, we interpolate the velocity at the boundary Lagrangian point with

$$\boldsymbol{u}_\ell(\boldsymbol{X}_k, t+\Delta t) = \sum_{\boldsymbol{x}} \boldsymbol{u}_\ell(\boldsymbol{x}, t+\Delta t) W(\boldsymbol{x}-\boldsymbol{X}_k)(\Delta x)^3. \tag{23}$$

Lastly, we correct the body force with

$$\boldsymbol{G}_{\ell+1}(\boldsymbol{X}_k, t+\Delta t) = \boldsymbol{G}_\ell(\boldsymbol{X}_k, t+\Delta t) - \frac{St}{\Delta t}\boldsymbol{u}_\ell(\boldsymbol{X}_k, t+\Delta t), \tag{24}$$

and repeat the steps using Eqs. (21)–(24) several times. From the preliminary computations, $\boldsymbol{G}_{\ell=6}(\boldsymbol{x}, t+\Delta t)$ is enough to keep no-slip condition on the boundary points. Therefore, we iterate the above procedure until $\ell = 6$ in the following computations.

3.3. Motion of particle and coupling with LBM

The first-order Euler method is used for the calculations of the motion of particles. During the time-step Δt, a particle P_j ($j = 1, 2, \ldots, N_\mathrm{p}$) at Lagrangian points $\boldsymbol{X}_j(t)$ moves to the following point:

$$\boldsymbol{X}_j(t+\Delta t) = \boldsymbol{X}_j(t) + \frac{\Delta t}{St}\boldsymbol{U}_j(t), \tag{25}$$

where $\boldsymbol{U}_j(t)$ is the velocity of the particle. The Lagrangian point $\boldsymbol{X}_j(t)$ generally differs from the Eulerian grid points. Then, the velocity $\boldsymbol{U}_j(t)$ is obtained by the weighted linear interpolation of the fluid velocities $\boldsymbol{u}(t)$ at the surrounding eight points in the cubic lattice.

At the same time, the displacement of the springs, surface area and total volume are changed, and the particle is subject to the elastic force $\boldsymbol{F}_j(t)$, as given by Eq. (3). In addition, because the Lagrangian point does not coincide with Eulerian grid points, $\boldsymbol{F}_j(t)$ is redistributed to the surrounding Eulerian grid points by the linear interpolation. The obtained elastic force $\boldsymbol{F}(t)$ at the Eulerian grid point $\boldsymbol{x}$ is substituted into the last term in the right-hand side of Eq. (11).

4. Results and discussion

4.1. Validation of RBC model

In order to confirm the validity of the RBC model, we calculate the motion of the body in a circular pipe flow. As shown in Fig. 5, the length and diameter of the pipe are $L_x = 100\Delta x$ and $D = 37.2\Delta x$, respectively, and a biconcave disk-shaped body whose initial longitudinal axis is $D_0 = 32\Delta x$ is placed on the centerline of the pipe. The membrane of the body consists of $N_\mathrm{p} = 258$ particles. The periodic boundary condition with pressure difference Δp is used at the inlet and outlet, and the no-slip boundary condition is used at walls of the pipe. The viscosities of the fluid phase A, the fluid phase B and the membrane are $\mu_\mathrm{FA} = 3.93 \times 10^{-2}\Delta x$, $\mu_\mathrm{FB} = \mu_\mathrm{M} = 9.42 \times 10^{-3}\Delta x$. The elastic moduli are determined so that $K^\mathrm{a} = K^\mathrm{A} = K^\mathrm{V} = \overline{K_m^\mathrm{l}}$, where $\overline{K_m^\mathrm{l}}$ is the arithmetic mean of K_m^l and set to $2.28 \times 10^{-5}(\Delta x)^3$. Note that the fluid properties such as the viscosity correspond to a specific case of human blood flow (Shiga, et al., 1990; Zhang, et al., 2009). The number of Lagrangian points at the boundary of the pipe is $N = 100$. The other parameters are the same as those in Murayama et al. (2011b). We perform the simulations for $0.04 \leq Re \leq 0.13$, where Re is the Reynolds number defined as $Re = \rho_\mathrm{FB} U_\mathrm{t} D_0/\mu_\mathrm{FB}$, with U_t being the terminal axial velocity of the body. Here, the velocity of the body means the velocity at the centroid of the membrane in the body.

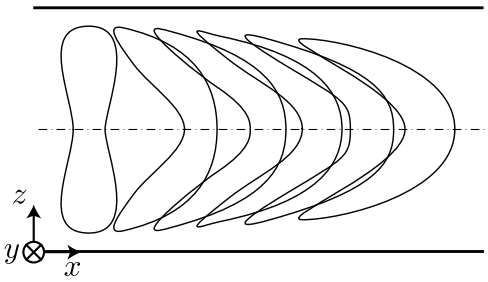

Fig. 6 Time evolution of body shape at $Re = 0.10$.

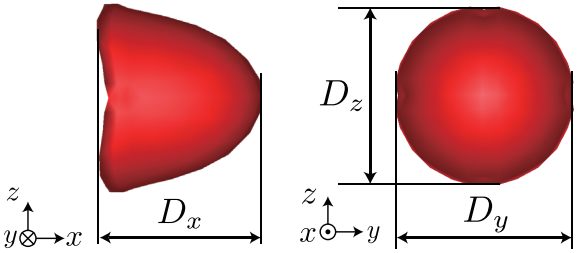

Fig. 7 Definition of lengths of deformed body in the x-, y- and z-directions.

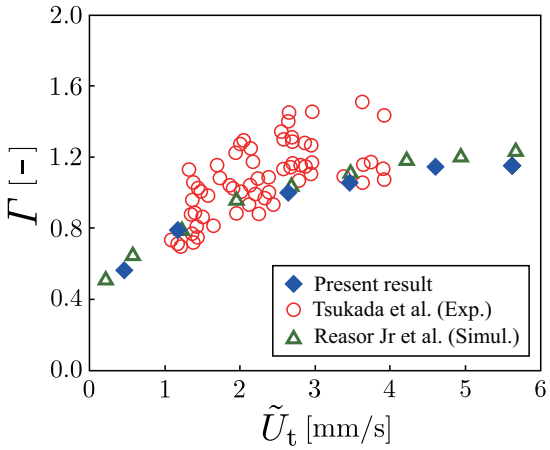

Fig. 8 Relation between deformation index Γ and dimensional terminal axial velocity $\tilde{U}_t$ at steady state: ♦, present result; ○, experiment by Tsukada et al. (2001); △, simulation by Reasor Jr et al. (2012).

Figure 6 shows time evolution of the cross-sectional shape of the body at $Re = 0.10$. It is seen that the body becomes deformed into axisymmetric parachute-like shape, and goes downstream around the centerline of the pipe. This shape is qualitatively similar to that observed in the experiment by Tsukada et al. (2001). Using the variables defined in Fig. 7, the deformation index Γ can be calculated as $\Gamma = 2D_x/(D_y + D_z)$, where D_x, D_y and D_z are the lengths of the body in the x-, y- and z-directions, respectively. Figure 8 shows the relation between the deformation index and the terminal axial velocity of the body at steady state. It should be noted that U_t is transformed into the dimensional velocity $\tilde{U}_t$ to compare with available experimental data and calculated values. It is seen that the present results are in good agreement with experimental data by Tsukada et al. (2001) and simulation results by Reasor Jr et al. (2012). Therefore, it is verified that the present RBC model can be applied to simulation of the motion of RBCs in microscale capillary blood vessels.

4.2. RBC motion in constricted pipe flow

As shown in Fig. 9, we consider a circular pipe and a square pipe, each of which has a constriction at the center of the domain. The entrance of the constriction is positioned at $x = L_p$. For the circular pipe, the diameters of the inlet and outlet are $D_{\max}$, the total length is L_x, the length and the minimum diameter of the constriction are $2L_s$ and $D_{\min}$, respectively,

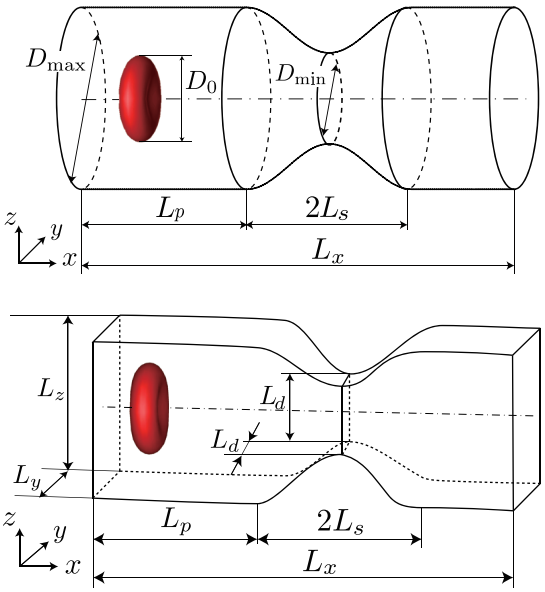

Fig. 9 Computational domains: circular pipe (upper); square pipe (lower).

and the diameter $D(x)$ of the constriction is determined by the following equation (Kozuma and Inamuro, 2011):

$$D(x) = \begin{cases} \dfrac{D_{\max}}{2}\left[1+\cos\left\{\dfrac{\pi}{L_s}(x-L_p)\right\}\right] + \dfrac{D_{\min}}{2}\left[1-\cos\left\{\dfrac{\pi}{L_s}(x-L_p)\right\}\right], & L_p \le x \le L_p + 2L_s \\ D_{\max}, & \text{otherwise.} \end{cases} \tag{26}$$

For the square pipe, the cross-sectional square of the inlet and outlet is $L_y \times L_y$ ($L_z = L_y$), the total length is $L_x = 2.39L_y$, and the length and the minimum side of the constriction are $2L_s$ and L_d, respectively. Also, the constriction side is determined using the same function as mentioned above by substituting L_y and L_d for $D_{\max}$ and $D_{\min}$, respectively.

The periodic boundary condition with pressure difference Δp is used at the inlet and outlet. The no-slip boundary condition is used at walls of the pipes. In the calculations, a biconcave disk-shaped body with initial longitudinal axis D_0 is placed on the centerline at $x = 0.1L_x$, and the motion of the body in pressure-driven flow is simulated. In particular, the effects of the pipe shape, of the constriction length and of the constriction size (the diameter of the cross-sectional circle) on the behavior of the body.

Computational parameters are as follows: $\rho_{\mathrm{FA}} = 1$, $\rho_{\mathrm{FB}} = 1$, $\mu_{\mathrm{FA}} = 3.93 \times 10^{-2}\Delta x$, $\mu_{\mathrm{FB}} = \mu_{\mathrm{M}} = 9.42 \times 10^{-3}\Delta x$, $K^{\mathrm{a}} = K^{\mathrm{A}} = K^{\mathrm{V}} = 2.28 \times 10^{-5}(\Delta x)^3$, $L_x = 105\Delta x$, $L_y = 49.6\Delta x$, $L_p = 40\Delta x$, $L_s = 10\Delta x$, $L_d = 19.2\Delta x$, $D_{\max} = 49.6\Delta x$, $D_{\min} = 19.2\Delta x$, $D_0 = 22\Delta x$, $N_{\mathrm{p}} = 258$, $N = 100$, and $\Delta p = 5.5 \times 10^{-6}$. The other parameters are the same as those in Murayama et al. (2011b). Note that the hydraulic equivalent diameters are used for L_y and L_d.

Grid convergence is checked for both Eulerian and Lagrangian grids. For Eulerian grid, the lattice resolutions and the number of particles in the membrane are determined by reference to the grid convergence test carried out in the previous paper (Murayama et al., 2011b). As an example, when we carried out one case of the simulations for the constricted circular pipe flow with 1.25 times finer grid, we found that the calculated results of the deformation index and the velocity were almost the same as the results with the standard grid. For Lagrangian grid in the IBM, on the other hand, preliminary computations were performed for several values of N (the number of Lagrangian points) in fundamental problems. The value of N used in the present simulations is determined from these results.

4.2.1. Effect of circular and square pipes We first compare the results in the circular and square pipe flows at $Re = 6.2 \times 10^{-3}$. Time evolutions of the body shape in the circular and square pipes with constriction are shown in Fig. 10. In both cases, it is seen that the body is elongated at the constriction and after passing through the constriction, the body becomes deformed into concave shape on the upstream and convex shape on the downstream like a parachute. Figure 11 shows time variations of the calculated deformation index Γ and the axial velocity u of the body. It should be noted that the velocity of the body represents the velocity at the centroid of the membrane in the body, and this definition is applied in the following figures. The dimensionless time is given by $t^* = mU_{\max}\Delta x/D_0$, where m is the number of time-step, and $U_{\max}$ is the maximum velocity in Poiseuille flow without a body. In both cases, the body becomes elongated in

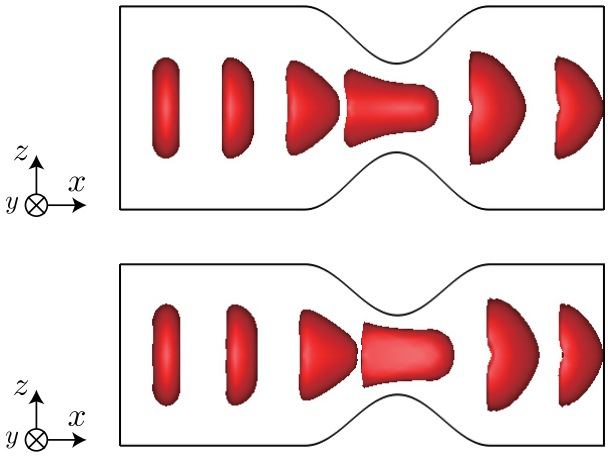

Fig. 10 Time evolutions of body shape: circular pipe (upper); square pipe (lower).

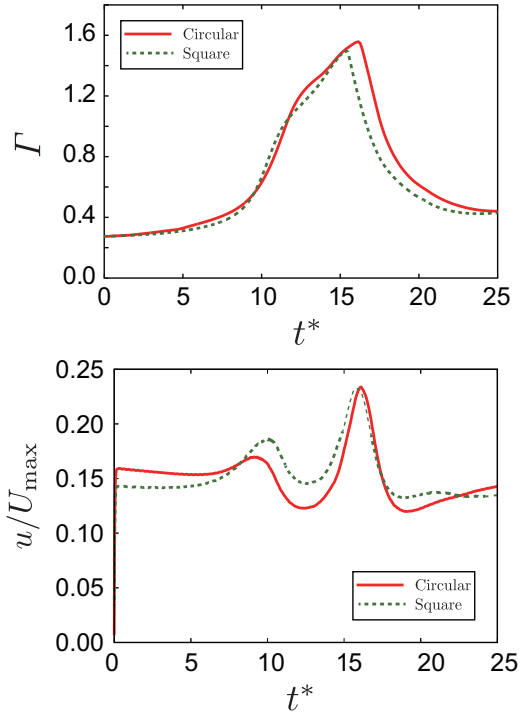

Fig. 11 Time variations of deformation index (upper) and axial velocity (lower) of the body in circular and square pipe flows ($t^* = mU_{\max}\Delta x/D_0$).

the x-direction when it passes through the constriction, and there are small and large peaks in the axial velocity profiles. Nevertheless, by comparison with these two results, it is found that the body in the circular pipe flow undergoes a little larger deformation and passes more slowly than in the case of square pipe flow. Also, time variation of the axial velocity in the circular pipe flow is larger than that in the square pipe flow. Therefore, from these results, it is considered that the body in the circular pipe flow is more affected by the constriction and that it takes more time to return to its equilibrium shape after the deformation than in the case of the square pipe flow.

4.2.2. Effect of length of constriction We next investigate the effect of the constricted length in the circular pipe on the behavior of the body. In the calculations, the constricted length is changed in the range of $0.455 \leq L_s/D_0 \leq 1.36$. The other parameters are the same as those in the previous section except for $D_{\min} = 22\Delta x$ in this case.

Figure 12 shows time variations of the deformation index and the axial velocity for various constricted lengths. In all cases, the body is deformed at the constriction by flow resistance and changed to an equilibrium shape. Also, the body is accelerated at the entrance and exit in the constriction, but reduces its speed while going through the constriction. In comparison with these cases, as the length L_s becomes smaller, the body is deformed larger and the axial velocity

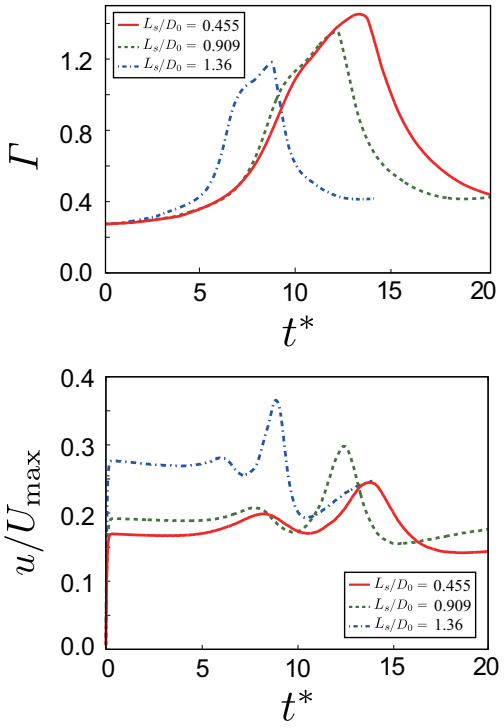

Fig. 12 Time variations of deformation index (upper) and axial velocity (lower) of the body in circular pipe flow for various constricted lengths ($t^* = mU_{\max}\Delta x/D_0$).

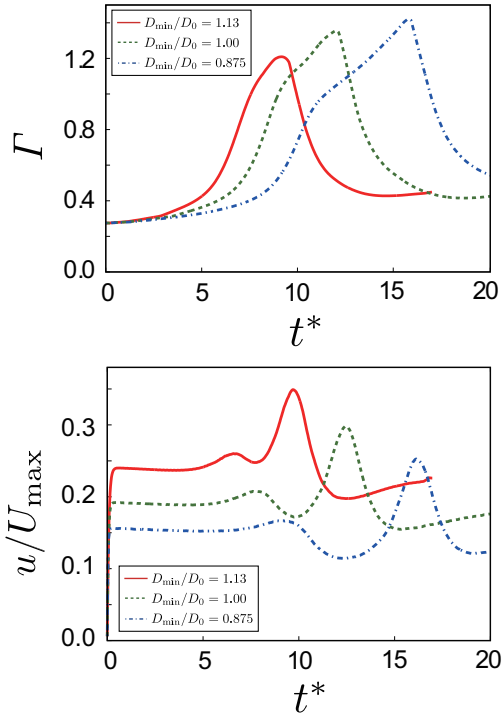

Fig. 13 Time variations of deformation index (upper) and axial velocity (lower) of the body in circular pipe flow for various minimum diameters of constriction ($t^* = mU_{\max}\Delta x/D_0$).

becomes smaller owing to abrupt decrease in the channel width. Moreover, reduction in the velocity indicates the loss of the kinetic energy of the body, and the drag exerted on the body is considered to be significant especially at steep constrictions. Calculation of the drag by summation of the force exerted on the triangular elements in the membrane (Omori et al., 2012) will be reported in future work.

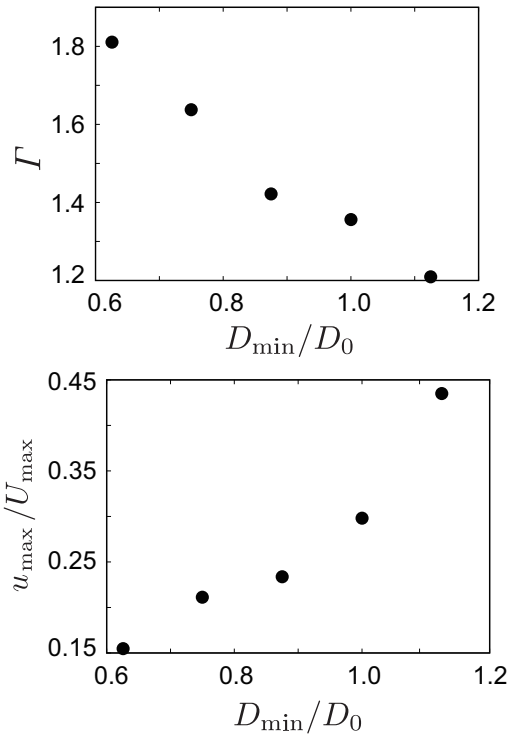

Fig. 14 Deformation index (upper) and maximum axial velocity (lower) against minimum diameters of constriction in circular pipe flow.

4.2.3. Effect of size of constriction We finally investigate the effect of the constricted size in the circular pipe on the behavior of the body. In the calculations, the minimum diameter of the constriction is changed in the range of $0.625 \leq D_{\min}/D_0 \leq 1.13$. The other parameters are the same as those in the previous section.

Time variations of the deformation index and the axial velocity for various minimum diameters of the constriction are shown in Fig. 13. Also, the deformation index and the maximum axial velocity $u_{\max}$ against the minimum diameter are shown in Fig. 14. It is found from these figures that as the minimum diameter becomes larger, the deformation index almost linearly reduces and the maximum axial velocity exponentially increases. On the other hand, as the minimum diameter becomes smaller, it is expected that the body is hard to pass through the pipe, and finally it may plug at the constriction, i.e., blocking the flow, as seen in the case of a droplet (Inamuro, 2012). Investigation into the critical conditions for the onset of the plugging is also an interesting issue.

5. Concluding remarks

The LBM for two-phase flows containing a deformable body with a viscoelastic membrane has been applied to the motion of a biconcave disk-shaped body in pressure-driven pipe flows. In particular, the characteristics of the body passing through a constriction have been investigated under various geometrical conditions. From these results, it is found that the present method has applicability to simulation of the motion of RBCs in microscale capillary blood vessels.

Finally, although the behavior of a single body has been investigated, the authors are now studying the motion of multi-bodies in pipe flows by dealing with the interaction between the bodies.

Acknowledgments

This work was partly supported by JSPS KAKENHI Grant Number 23560192. The authors thank Dr. Kosuke Suzuki for helpful discussion in the revised manuscript.

References

Chen, S. and Doolen, G.D., Lattice Boltzmann method for fluid flows, Annual Review of Fluid Mechanics, Vol.30 (1998), pp.329-364.

Dupin, M.M., Halliday, I., Care, C.M. and Munn, L.L., Lattice Boltzmann modelling of blood cell dynamics, International Journal of Computational Fluid Dynamics, Vol.22, No.7 (2008), pp.481-492.

Dzwinel, W., Boryczko, K. and Yuen, D.A., A discrete-particle model of blood dynamics in capillary vessels, Journal of Colloid and Interface Science, Vol.258, No.1 (2003), pp.163-173.

Evans, E.A., Minimum energy analysis of membrane deformation applied to pipet aspiration and surface adhesion of red blood cells, Biophysical Journal, Vol.30, No.2 (1980), pp.265-284.

Fischer, T.M, Stöhr-Lissen, M. and Schmid-Schönbein, H., The red cell as a fluid droplet: tank tread-like motion of the human erythrocyte membrane in shear flow, Science, Vol.202, No.4370 (1978), pp.894-896.

Hochmuth, R.M., Marple, R.N. and Sutera, S.P., Capillary blood flow: I. Erythrocyte deformation in glass capillaries, Microvascular Research, Vol.2, No.4 (1970), pp.409-419.

Imai, Y., Kondo, H., Ishikawa, T., Lim, C.T. and Yamaguchi, T., Modeling of hemodynamics arising from malaria infection, Journal of Biomechanics, Vol.43, No.7 (2010), pp.1386-1393.

Inamuro, T., Tomita, R. and Ogino, F., Lattice Boltzmann simulations of drop deformation and breakup in shear flows, International Journal of Modern Physics B, Vol.17, Nos.1-2 (2003), pp.21-26.

Inamuro, T., Lattice Boltzmann methods for viscous fluid flows and for two-phase fluid flows, Fluid Dynamics Research, Vol.38, No.9 (2006), pp.641-659.

Inamuro, T., Lattice Boltzmann methods for moving boundary flows, Fluid Dynamics Research, Vol.44, No.2 (2012), 024001.

Koshizuka, S. and Oka, Y., Moving-particle semi-implicit method for fragmentation of incompressible fluid, Nuclear Science and Engineering, Vol.123, No.3 (1996), pp.421-434.

Kozuma, T. and Inamuro, T., Numerical simulations of the behavior of a droplet moving in a constricted tube by the lattice Boltzmann method, Proceedings of the 25th CFD Symposium (2011), E04-2. (in Japanese)

Murayama, T., Yoshino, M. and Hirata, T., Two-phase lattice Boltzmann simulation of behavior of a body with a viscoelastic membrane in fluid flows (Effect of internal fluid viscosity on body behavior), Transactions of the Japan Society of Mechanical Engineers, Series B, Vol.77, No.773 (2011a), pp.4-19. (in Japanese)

Murayama, T., Yoshino, M. and Hirata, T., Three-dimensional lattice Boltzmann simulation of two-phase flow containing a deformable body with a viscoelastic membrane, Communications in Computational Physics, Vol.9, No.5 (2011b), pp.1397-1413.

Omori, T., Ishikawa, T., Barthès-Biesel, D., Salsac, A.-V., Imai, Y. and Yamaguchi, T., Tension of red blood cell membrane in simple shear flow, Physical Review E, Vol.86, No.5 (2012), 056321.

Peskin, C.S., Numerical analysis of blood flow in the heart, Journal of Computational Physics, Vol.25, No.3 (1977), pp.220-252.

Peskin, C.S., The immersed boundary method, Acta Numerica, Vol.11 (2002), pp.479-517.

Ramanujan, S. and Pozrikidis, C., Deformation of liquid capsules enclosed by elastic membranes in simple shear flow: large deformations and the effect of fluid viscosities, Journal of Fluid Mechanics, Vol.361 (1998), pp.117-143.

Reasor Jr, D.A., Clausen, J.R. and Aidun, C.K., Coupling the lattice-Boltzmann and spectrin-link methods for the direct numerical simulation of cellular blood flow, International Journal for Numerical Methods in Fluids, Vol.68, No.6 (2012), pp.767-781.

Rothman, D.H. and Zaleski, S., Lattice-Gas Cellular Automata (1997), Cambridge University Press.

Shiga, T., Maeda, N. and Kon, K., Erythrocyte rheology, Critical Reviews in Oncology/Hematology, Vol.10, No.1 (1990), pp.9-48.

Sone, Y., Asymptotic theory of flow of rarefied gas over a smooth boundary II, In: Dini, D. (Ed.), Rarefied Gas Dynamics, Vol.2 (1971), Editrice Tecnico Scientifica, Pisa, pp.737-749.

Succi, S., The Lattice Boltzmann Equation for Fluid Dynamics and Beyond (2001), Oxford University Press.

Sui, Y., Chew, Y.T., Roy, P. and Low, H.T., A hybrid method to study flow-induced deformation of three-dimensional capsules, Journal of Computational Physics, Vol.227, No.12 (2008), pp.6351-6371.

Suzuki, K. and Inamuro, T., Effect of internal mass in the simulation of a moving body by the immersed boundary method, Computers & Fluids, Vol.49, No.1 (2011), pp.173-187.

Tsubota, K., Wada, S. and Yamaguchi, T., Particle method for computer simulation of red blood cell motion in blood flow, Computer Methods and Programs in Biomedicine, Vol.83, No.2 (2006), pp.139-146.

Tsukada, K., Sekizuka, E., Oshio, C. and Minamitani, H., Direct measurement of erythrocyte deformability in diabetes mellitus with a transparent microchannel capillary model and high-speed video camera system, Microvascular Re-

search, Vol.61, No.3 (2001), pp.231-239.
Wada, S. and Kobayashi, R., Numerical simulation of various shape changes of a swollen red blood cell by decrease of its volume, Transactions of the Japan Society of Mechanical Engineers, Series A, Vol.69, No.677 (2003), pp.14-21. (in Japanese)
Wang, Z., Fan, J. and Luo, K., Combined multi-direct forcing and immersed boundary method for simulating flows with moving particles, International Journal of Multiphase Flow, Vol.34, No.3 (2008), pp.283-302.
Wolf-Gladrow, D.A., Lattice-Gas Cellular Automata and Lattice Boltzmann Models (2000), Springer.
Yoshino, M. and Murayama, T., A lattice Boltzmann method for a two-phase flow containing solid bodies with viscoelastic membranes, European Physical Journal Special Topics, Vol.171, No.1 (2009), pp.151-157.
Zhang, J., Johnson, P.C. and Popel, A.S., Effects of erythrocyte deformability and aggregation on the cell free layer and apparent viscosity of microscopic blood flows, Microvascular Research, Vol.77, No.3 (2009), pp.265-272.